Applied Catalysis B: Environmental 203 (2017) 465–474

Contents lists available at ScienceDirect

Applied Catalysis B: Environmental

journal homepage: www.elsevier.com/locate/apcatb

Chlorine intercalation in graphitic carbon nitride for efficient photocatalysis

Chengyin Liu [a], Yihe Zhang [a,*], Fan Dong [b], A.H. Reshak [c], Liqun Ye [d], Nicola Pinna [e], Chao Zeng [a], Tierui Zhang [f], Hongwei Huang [a,*]

[a] Beijing Key Laboratory of Materials Utilization of Nonmetallic Minerals and Solid Wastes, School of Materials Science and Technology, China University of Geosciences, Beijing 100083, PR China
[b] College of Environmental and Biological Engineering, Chongqing Technology and Business University, Chongqing 400067, China
[c] New Technologies—Research Centre, University of West Bohemia, Univerzitni 8, 306 14 Pilsen, Czech Republic and School of Material Engineering, University Malaysia Perlis, Kangar, Perlis, 01007, Malaysia
[d] Key Laboratory of Ecological Security for Water Source Region of Mid-line Project of South-to-North Water Diversion of Henan Province, College of Chemistry and Pharmaceutical Engineering, Nanyang Normal University, Nanyang 473061, China
[e] Institut für Chemie, Humboldt-Universität zu Berlin, Brook-Taylor-Strasse 2, 12489 Berlin, Germany
[f] Key Laboratory of Photochemical Conversion and Optoelectronic Materials, Technical Institute of Physics and Chemistry, Chinese Academy of Sciences, Beijing 100190, China

ARTICLE INFO

Article history:
Received 19 August 2016
Received in revised form
26 September 2016
Accepted 3 October 2016
Available online 6 October 2016

Keywords:
Photocatalysis
Visible light
Cl intercalation
Interlayer pathway
Charge transfer

ABSTRACT

Metal-free graphitic carbon nitride (g-C_3N_4) shows tremendous potentials in energy and environmental domains. Nonetheless, amelioration on the crystal configuration, electronic structure and microstructure of g-C_3N_4 for high-performing visible-light photocatalysis is still challenging and anticipated. Here we report the development of chlorine (Cl) intercalated g-C_3N_4 via co-pyrolysis of melamine and excessive ammonium chloride (excessive is very pivotal). This protocol renders not only Cl intercalation in the interlayer of g-C_3N_4, but also a homogeneous porous structure, thereby endowing g-C_3N_4 with multiple superiority effects, including significantly promoted charge migration by establishing interlayer pathway, up-shifted conduction-band level, narrowed band gap as well as enhanced surface area. The as-prepared Cl intercalated mesoporous g-C_3N_4 parades outstanding photocatalytic performance for water splitting into H_2, CO_2 reduction, liquid and air contaminants removal. The most enhanced photocatalytic performance was obtained at Cl-C_3N_4-3 for H_2 evolution activity, which shows a 19.2-fold increase in contrast to pristine g-C_3N_4, accompanying with a high apparent quantum efficiency of 11.9% at 420 ± 15 nm. Experimental and DFT calculations results co-disclose that the aforementioned advantageous factors account for the profoundly boosted photooxidation and photoreduction capabilities of g-C_3N_4 under visible light. The present work may furnish a bottom-up tactic for integrally advancing g-C_3N_4, and also hold huge promise to be extended to other layered materials for photochemical or photoelectrochemical applications.

1. Introduction

Two-dimensional (2D) layered materials have gained considerable interests owing to their unique 2D confined structure, which enables exotic properties for multiple applications in energy generation and storage [1], sensor [2], catalysis [3] and electronics [4]. Graphitic carbon nitride (g-C_3N_4), as a nontoxic metal-free and easily available layered material, shows huge capabilities for photocatalytic hydrogen evolution [3], contaminant elimination [5] and CO_2 reduction [6]. Nonetheless, the photocatalytic performance of g-C_3N_4 is restricted by the low quantum efficiency derived from its slow charge mobility and fast recombination of charge carriers. To remedy these drawbacks, various attempts have been made, such as building sundry nanoarchitectures [7], surface modification [8], fabrication of heterojunction [9] and doping with chemical elements [10–16]. Among the above-mentioned strategies, doping is proved to be an absorbing way to modulate the electronic structure of g-C_3N_4, achieving fine tailoring on the band gap and photocatalytic activity. Unfortunately, doping of g-C_3N_4 with non-metal elements such as C, B, P, S, F and O, involves replacement of lattice atoms (C or N) by these elements [10–14]. The incorporation of metals such as Cu^{2+}, Fe^{3+}, Co^{3+}, and Ni^{2+} into g-C_3N_4 only allows them

* Corresponding authors.
E-mail addresses: zyh@cugb.edu.cn (Y. Zhang), hhw@cugb.edu.cn (H. Huang).

http://dx.doi.org/10.1016/j.apcatb.2016.10.002
0926-3373/

to be located in the cavities among adjacent tri-s-triazine units on the same π-conjugated planes [15,16]. All in all, these efforts failed to improve the charge transfer between tri-s-triazine textural conjugated planes. Moreover, through these approaches it was not possible to move from van der Waals stacked g-C_3N_4 sheets to covalently bonded sheets. Based on these findings, it appears that the introduction of species promoting covalently bonding between g-C_3N_4 sheets would be the way to follow. Indeed it would allow an efficient charge migration between sheets, simultaneously achieving the band structure modulation.

It was lately demonstrated by Xiong. et al. [17] that the K atoms can be intercalated into the space between the g-C_3N_4 layers, which could decrease the electronic localization and extend the π conjugated system, thus enabling g-C_3N_4 highly enhanced visible-light photocatalytic performance for NO removal. Given these benefits, g-C_3N_4 intercalation modification may represent a new promising orientation for boosting the photocatalytic performance of g-C_3N_4 in future. However, so far little information about intercalated g-C_3N_4 is available, and microstructure amelioration has not been achieved in intercalated g-C_3N_4. In particular, the photoreduction ability for generating renewable energy (water splitting for H_2 production, CO_2 reduction, etc.) of intercalated g-C_3N_4 is urgent to be probed.

Recently, Lu et al. [18] prepared g-C_3N_4 nanosheets using 2 g of dicyanodiamide powder and 10 g ammonium chloride as raw materials. Though thin-layered g-C_3N_4 was obtained, the Cl doping/intercalation and porous structure were not observed. Wan et al. [19] prepared Cl doped g-C_3N_4 and characterized its photocatalytic performance for Rhodamine B degradation. Nonetheless, the location of doped Cl atoms is unclear, and the mechanism on activity enhancement is poorly understood. Considering the handicaps that severely confine the efficiency of bulk g-C_3N_4, such as slow charge mobility, lack of reactive reaction sites, weak photoabsorption, etc. it may be feasible to develop a suitable intercalation approach to eliminate all the aforementioned disadvantages simultaneously.

In this work, we present the synthesis of chlorine (Cl) intercalated g-C_3N_4 via a facile soaking-copyrolysis strategy of melamine and enormous amount of ammonium chloride. Herein, the substantial ammonium chloride not only provides Cl source for intercalation in the interlayer of g-C_3N_4, but also offers gas soft-template to produce porous structure. By employing systematical characterization techniques and density functional theory (DFT) calculation, we investigate the effects of Cl intercalation on the crystal configuration, electronic structure, microstructure as well as the charge movement behaviors of g-C_3N_4. It is fascinating to find that Cl intercalated g-C_3N_4 possesses multiform favorable properties, such as significantly promoted charge transport by establishing interlayer pathways, more negative conduction-band level, narrowed band gap and increased specific surface area. Benefited from the above advantages, the Cl intercalated g-C_3N_4 exhibits enhanced photocatalytic activity toward H_2 production, CO_2 reduction, degradation of azo dye and air contaminant. This treatment opens up a new avenue for developing absorbing g-C_3N_4-based materials with prominent all-round photocatalytic performance.

2. Experimental section

2.1. Synthesis

Melamine (4 g) and ammonium chloride (their molar ratios were separately 1:0, 1:5, 1:20, 1:30, 1:40) were completely mixed in deionized water and kept stirring for 24 h, and then allowed to remove water at 90 °C. Then the precursors were heated in muffle furnace at 520 °C for 4 h, and the chlorine (Cl) intercalated g-C_3N_4 photocatalysts were obtained. These samples are donated as g-C_3N_4 and Cl-C_3N_4-1, Cl-C_3N_4-2, Cl-C_3N_4-3 and Cl-C_3N_4-4.

2.2. Characterization

The morphologies of the photocatalysts were analyzed by field emission scanning electron microscopy (SEM) on a Hitachi S-4800 instrument. The microstructure of samples was examined by transmission electron microscopy (TEM; JEM-2100, Japan). The samples were characteristic by X-ray powder diffraction (XRD), the Bruker D8 focus Advance diffractometer with Cu-Kα radiation (40 kV/40 mA). Fourier transform infrared spectroscopy (FTIR) spectra were obtained by a Bruker spectrometer in a KBr pellet and the frequency range was 4000 cm^{-1}–450 cm^{-1}. The UV–vis diffuse reflectance spectra (DRS) procured from the Varian Cary 5000 UV–vis spectrophotometer. X-ray photoelectron spectroscopy (XPS) was accustomed to examine the surface properties of samples, with Al Ka X-rays (ht: 1486.6 eV) irradiation operating at 150 W (XPS: Thermo ESCALAB 250, USA). The Brunauer-Emmett-Teller (BET) specific surface areas of samples were analyzed by nitrogen adsorption-desorption (Micromeritics ASAP 2460, USA). The photoluminescence spectra (PL) spectra were recorded by a fluorescence spectrophotometer (Hitachi F- 4600) made in Japan, with a 150 W Xe lamp at 400 V as the excitation lamp. The fluorescence decay spectra were measured by the fluorescence decay spectrometer (HORIBA, JOBIN YVON FL3-21), and 370 nm pulse laser radiation (nano-LED) was as the excitation source with the pulse width of the laser 12 ns.

2.3. Photodegradation evaluation

Photocatalytic activities of samples were evaluated by degradation of RhB in an aqueous solution under visible light (λ > 420 nm) irradiation of a 500 W Xenon lamp. 50 mg of the powder photocatalyst was dispersed into 50 mL of RhB (0.01 mM) solution. Before illumination, the mixture was placed in quartz tube and ultraphonic stirred about 10 min, then the suspensions were magnetic stirring in dark for 0.5 h to earn the adsorption-desorption equilibrium. After, those mixture solutions were illuminated under visible light and 2.5 mL of the suspension was taken and centrifugalized at a certain period time. The UV–vis spectrophotometers of the centrifuged solution were recorded using a Cary 5000 spectrophotometer.

2.4. Photocatalytic H_2 evolution

Photocatalytic H_2 production experiments were performed in photoreactor (Pyrex glass) at room temperature connected to a closed-cycle gas circulation system. A 300 W Xe lamp with optical filter (λ > 420 nm) was used as light source. In a typical photocatalytic experiment, 50 mg of photocatalyst powder was suspended in 20 mL of distilled water and 10 mL lactic acid with the loading of 3 wt% Pt cocatalyst, which was conducted by directly dissolving H_2PtCl_6 into the above suspension. Before photocatalytic experiments, the aqueous solution was bubbled by nitrogen for 15 min to remove dissolved oxygen. Then, the suspension solution was stirred and irradiated (UV-light) for 30 min and entered into photoreactor with 70 mL distilled water finally. The products were analyzed by gas chromatography (Labsolar-III(AG), high-purity nitrogen as a carrier gas) using a thermal conductivity detector.

The apparent quantum efficiency (AQE) for hydrogen production was measured using the wavelength of 420, 450, 550 and 600 nm band-pass filters. The AQE was calculated by the following equation:

AQY (%) = number of evolved H_2 molecules × 2 × 100/number of incident photons

2.5. Photocatalytic CO_2 reduction

The photoreduction of CO_2 conversion was carried out by a Labsolar-III AG closed circulation system (Beijing Perfect light Technology Co., Ltd., China). 0.05 g as-prepared photocatalyst and 1.3 g $NaHCO_3$ were uniformly dispersed on a glass sheet placed in a reaction cell. Subsequently, 5 mL H_2SO_4 (4 M) was transfused into the vacuum reactor to react with $NaHCO_3$ to obtain 1 atm CO_2 gas. The reactor was irradiated by a 300 W Xe lamp with a filter ($\lambda > 420$ nm), and photoreaction temperature kept at 20 °C. After, 1 mL of gas was taken for subsequent qualitative analysis by GC9790II gas chromatography (Zhejiang Fuli Analytical Instrument Co.) with a thermal conductivity detector.

2.6. Photocatalytic removal NO

The photocatalytic activity of NO removal was performed by a chemiluminescence NO analyzer (Thermo Environmental Instruments Inc., 42i-TL). 0.20 g as-prepared photocatalyst dispersed in 50 mL distilled water and ultrasonic treatment for 15 min, then coated two glass dishes with 12 cm diameter. The dishes put into a 4.5 L (30 cm × 15 cm × 10 cm) reactor made of stainless steel and Saint-Glass. A 150 W lamp with a 420 nm filter was placed above the reactor. The NO gas was 600 ppb, which was diluted from the concentration of 100 ppm by air stream.

2.7. Photoelectrochemical measurements

Photoelectrochemical measurements were consist of photocurrent (PC) and electrochemical impedance spectra (EIS), which were measured by a three-electrode system with visible light on and off, and the light intensity was 1 mW/cm^2 with Na_2SO_4 (0.1 M) as the electrolyte solution at 0.0 V. The saturated calomel electrodes (SCE) were used as the reference electrode, and the platinum wires were as the counter electrode. The working electrodes were pristine g-C_3N_4 and modified g-C_3N_4 film electrodes. A 5 mV sinusoidal AC perturbation was used to the electrode over the frequency range of 0.05–10^5 Hz. The Mott-Schottky curves were gauged at a frequency of 100 Hz in 0.1 M Na_2SO_4 aqueous solution.

2.8. Active species trapping experiment

The active species trapping were ethylenediaminetetraacetic acid disodium salt (EDTA-2Na), Benzoquinone (BQ), and isopropanol (IPA), which were introduced as the scavengers to detect holes (h^+), superoxide radicals ($\bullet O_2^-$) and hydroxyl radicals ($\bullet$OH), respectively. The experiment was analyzed by 1 mM scavengers to degrade RhB in an aqueous solution under visible light ($\lambda > 420$ nm).

2.9. Density functional theory (DFT) calculation

To investigate the crystal structure of chlorine atom embedding g-C_3N_4, DFT calculations were carried out by exploiting the "Vienna ab initio simulation package" (VASP5.2) and Perdew–Burke–Ernzerhof function. For the total and partial density of state (DOS) k-points were adopted in $5 \times 5 \times 3$ Monkhorst-Pack grid, and the energy cut off was chosen as 450 eV [20,21].

3. Results and discussion

Scheme 1 displays the schematic synthetic process of chlorine-promoted g-C_3N_4. To incorporate Cl into the g-C_3N_4 structure, melamine (precursor of g-C_3N_4) is soaked in highly concentrated ammonium chloride solutions for 1 d. Then, it was allowed to be dried and pyrolyzed to obtain Cl intercalated g-C_3N_4 (Cl-g-C_3N_4) samples. Herein, the excessive ammonium chloride acts as not only chlorine source to offer Cl element, but also a foaming agent rendering g-C_3N_4 porous structure.

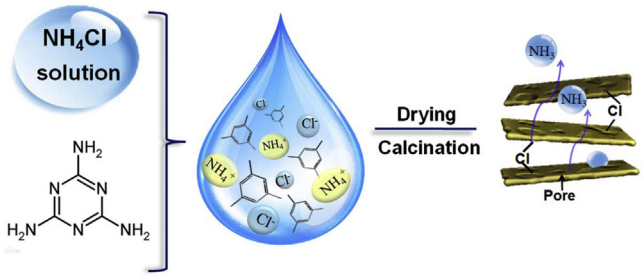

Scheme 1. Schematic illustration of the preparation for Cl intercalated g-C_3N_4 (Cl-g-C_3N_4) samples.

Table 1
Comparison for unit cell parameters of g-C_3N_4 and Cl-C_3N_4.

Parameters	a (Å)	b (Å)	c (Å)	α(°)	β(°)	γ(°)
g-C_3N_4	7.131	7.131	13.582	90	90	120
Cl-C_3N_4	7.209	7.215	13.734	89.999	89.415	120.025

XPS was performed to confirm the existence of Cl and to analyze the chemical environment of C and N upon Cl-promotion. As shown in Fig. 1a, an evidently extra Cl peak (inset) is observed in modified g-C_3N_4 compared with pristine g-C_3N_4. The Cl 2p spectra can be fitted into two peaks at 200.4 and 199.1 eV, which are separately assigned to Cl 2p1/2 and Cl 2p3/2, respectively [22], indicating the successful introduction of Cl into g-C_3N_4. High-resolution spectra of C 1s (Fig. 1b) and N 1s (Fig. 1c) reveal that N 1s band undergoes an obvious binding-energy shift, demonstrating that their chemical environments are affected. Density functional theory (DFT) calculation was applied to study the local structure of Cl-g-C_3N_4. In contrast to the doping of other non-metals or metals, such as C, N, B, O, S, Fe, Ni, Cu, etc., which reside on the π-conjugated planes of g-C_3N_4 [10–16], it is interesting to find that Cl atoms are located at the interlayers of g-C_3N_4 after crystal structure optimization and covalently bonded to the g-C_3N_4 acting as a bridge between sheets (Fig. 1d). The bridged Cl is believed to be favorable for the charge transfer process. Besides, the Cl embedding results in the enlargement of lattice parameters as shown in Table 1.

XRD patterns were employed to investigate the crystalline phase and Cl status of Cl-g-C_3N_4 series (Fig. S1). Obviously, Cl decoration does not alter the crystalline phase of g-C_3N_4, and all the XRD peaks are well indexed into the tetragonal phase of g-C_3N_4 (JCPDS No. 87-1526). The (002) peak at about 27.5° reflects the stacking of conjugated hexatomic rings of g-C_3N_4 along c axis with an interlayer distance of 0.339 nm [23]. Compared with the pristine g-C_3N_4, it can be seen that the (002) diffraction peak of Cl-g-C_3N_4 exhibits a left-shift in the XRD pattern (Fig. 2a). The slow-scanned XRD data (Fig. S2) also demonstrated that (002) peak of g-C_3N_4 undergoes a gradual shift from 27.45° to 27.31° with increasing the doped Cl amount. It indicates that the interlayer distance of g-C_3N_4 is enlarged by Cl decoration, namely an increase of the lattice parameters, which is consistent with the regular XRD results and the above DFT result. Fig. 2b shows the FTIR spectra of series samples. The FTIR peaks at 807 and 1243 cm^{-1} separately correspond to the triazine units and stretching vibration of C—N [24], which slightly shift toward high frequencies, suggesting that the coordination environment of C—N covalent bonds changes. These findings support the conclusion that Cl is successfully intercalated and covalently bonded to g-C_3N_4 sheets.

Fig. 3a–c presents representative TEM images of pristine g-C_3N_4 and Cl-C_3N_4. The pristine g-C_3N_4 exhibits bulk structures with

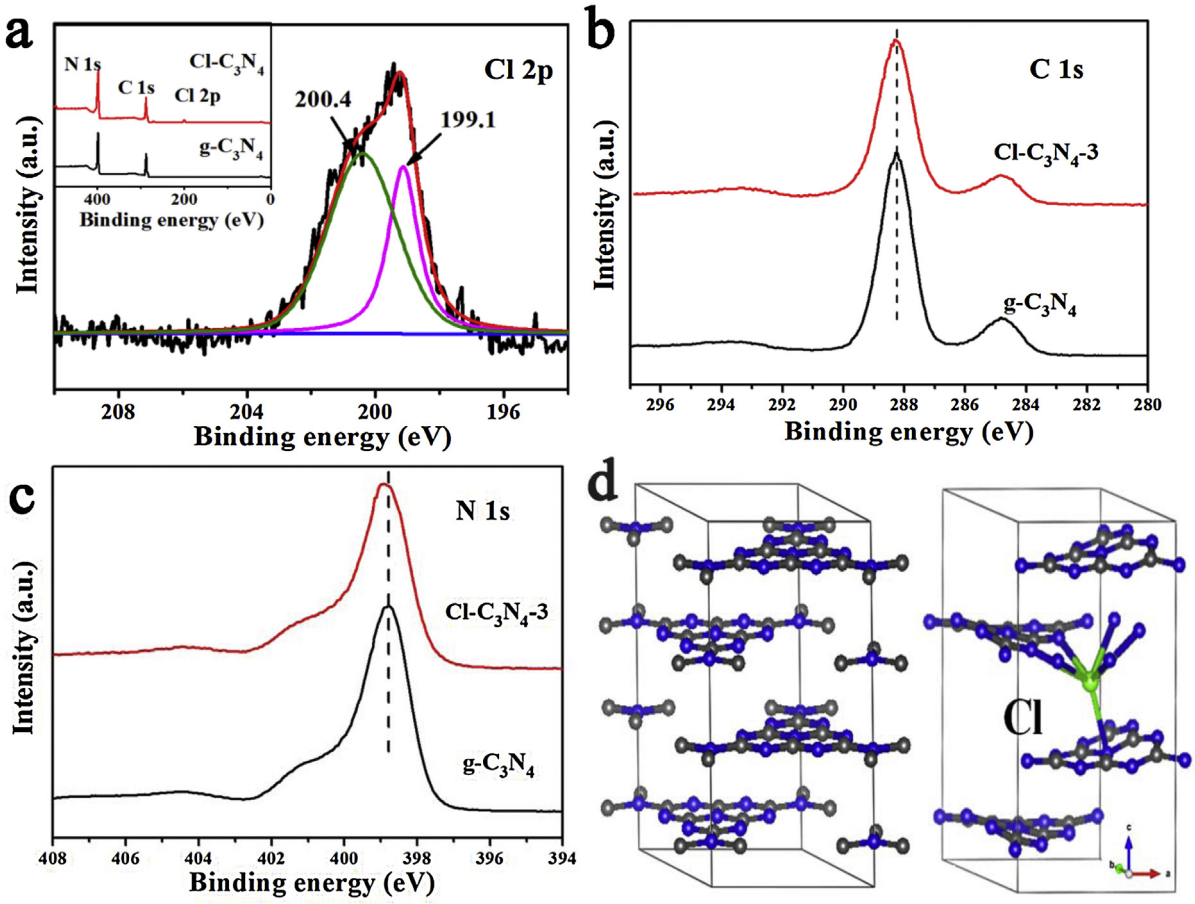

Fig. 1. (a) XPS survey spectra and Cl 2p. High resolution XPS spectra of (b) C 1s and (c) N 1s. (d) Crystal structure of pristine g-C_3N_4 and Cl-doped g-C_3N_4.

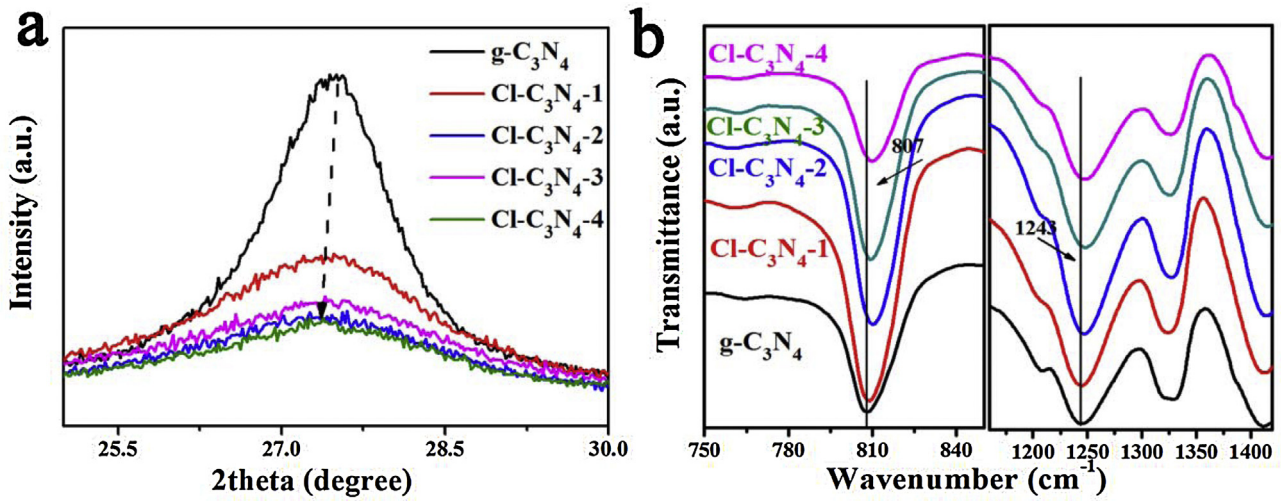

Fig. 2. (a) Enlarged XRD patterns of g-C_3N_4 and Cl-C_3N_4-X (X = 1, 2, 3, 4). (b) FTIR spectra of g-C_3N_4 and Cl intercalated g-C_3N_4 samples.

smooth surface (Fig. 3a). It is clear to see that the introduction of Cl has significant influence on the morphology of g-C_3N_4 (SEM of Fig. S3), and the g-C_3N_4 bulk samples can be corroded and form regular pores, which are uniformly distributed on the Cl-C_3N_4 slice with average diameter of ~30 nm (Fig. 3c). The porous net structure of Cl-C_3N_4 is supposed to have larger specific surface area (see below) and more reactive reaction sites, favoring photochemical reactions. Elemental mapping of Cl-C_3N_4 reveals that C, N, and Cl are detected and homogeneously distributed over the entire structure (Fig. 3d–f). It further confirms the Cl doping in the modified g-C_3N_4. To rule out the existence of NH_4Cl in the as-prepared samples, thermogravimetric (TG) of NH_4Cl was conducted. As seen from Fig. S4, NH_4Cl completely decomposes before 340 °C, which excludes the existence of NH_4Cl in Cl intercalated g-C_3N_4 sample.

Diffuse reflectance spectra of pristine g-C_3N_4 and Cl-C_3N_4 series are shown in Fig. 4a. The optical absorption of these samples is all enhanced and the regions can be divided into two parts corresponding to different reasons: Part I, 200–400 nm; Part II, >400 nm.

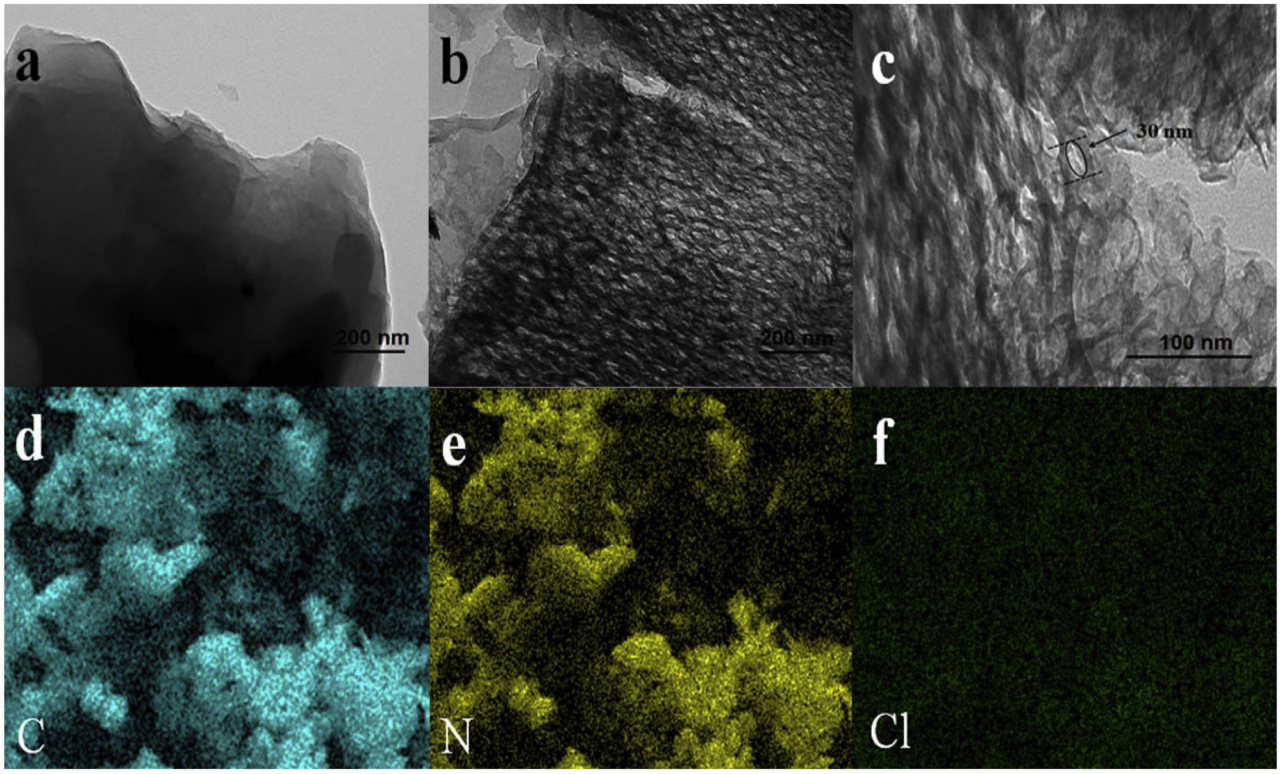

Fig. 3. TEM images of (a) g-C_3N_4, (b) Cl-C_3N_4, (c) the enlarge image of Cl-C_3N_4. Elemental mapping of (d) C, (e) N and (f) Cl.

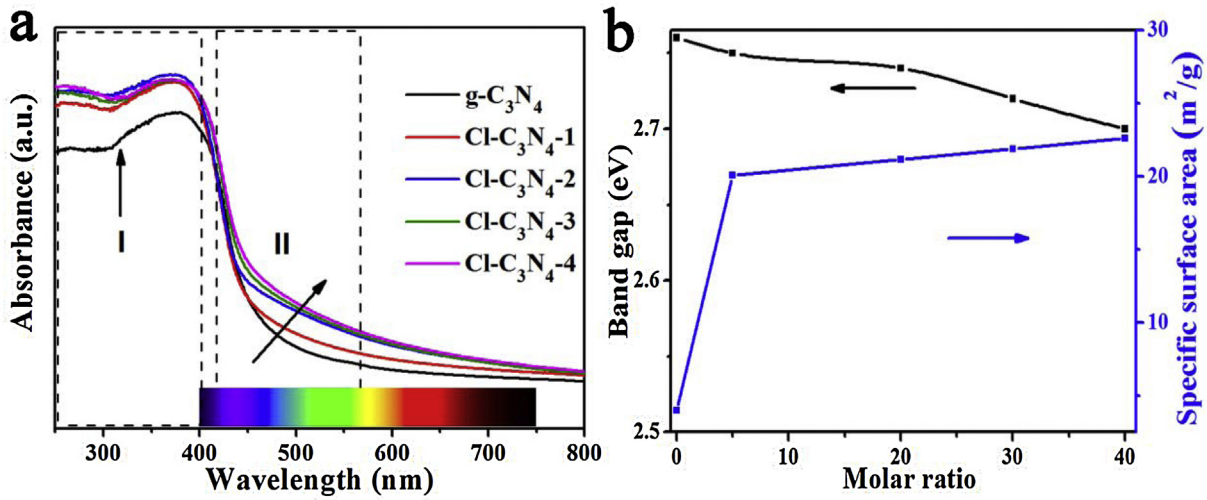

Fig. 4. (a) UV–vis diffuse reflectance spectra of g-C_3N_4 and Cl-C_3N_4 samples. (b) Plots of specific surface area and optical band gap vs. molar ratio of ammonium chloride to melamine.

It is important to notice that, in comparison to pristine g-C_3N_4, for part I, the enhanced photoabsorption of Cl-C_3N_4 may be ascribed to its porous nanostructure, which causes multiple reflection and scattering [25]. Whereas, the orderly strengthened optical absorption in part II is due to the narrowed band gap derived from the band structure alteration induced by Cl intercalation. Band gap of semiconductors can be determined by the formula $\alpha h\nu = A(h\nu - Eg)^{n/2}$ [26]. For the indirect optical transition of g-C_3N_4, the band gaps of g-C_3N_4 and Cl-C_3N_4-X (X = 1, 2, 3, 4) are calculated (from the plot of absorption1/2 versus energy) to be 2.76, 2.75, 2.74, 2.72 and 2.70 eV, respectively. As a result, it is clearly to see that the band gap of g-C_3N_4 is continuously narrowed because of Cl intercalation (black line in Fig. 4b and Fig. S5), which is beneficial to generating more photoexcitons. On the other hand, the specific surface area of g-C_3N_4 is drastically increased (up to 5 times) due to the porous structure of Cl intercalated g-C_3N_4 (blue line in Fig. 4b and Table S1). The significantly improved specific surface area would provide more active sites to accelerate photocatalytic reactions [27].

The influence of Cl intercalation on the photoreduction and photooxidation properties of g-C_3N_4 is evaluated by photocatalytic hydrogen evolution, CO_2 reduction, photodecomposition of azo dye model RhB and NO contaminants under visible light irradiation ($\lambda > 420$ nm). The photocatalytic H_2 evolution from water splitting over g-C_3N_4 and series of Cl-C_3N_4 samples is studied (Fig. 5a). Pristine g-C_3N_4 exhibits a low H_2 production rate, while the entire Cl-C_3N_4 samples exhibit drastically promoted evolu-

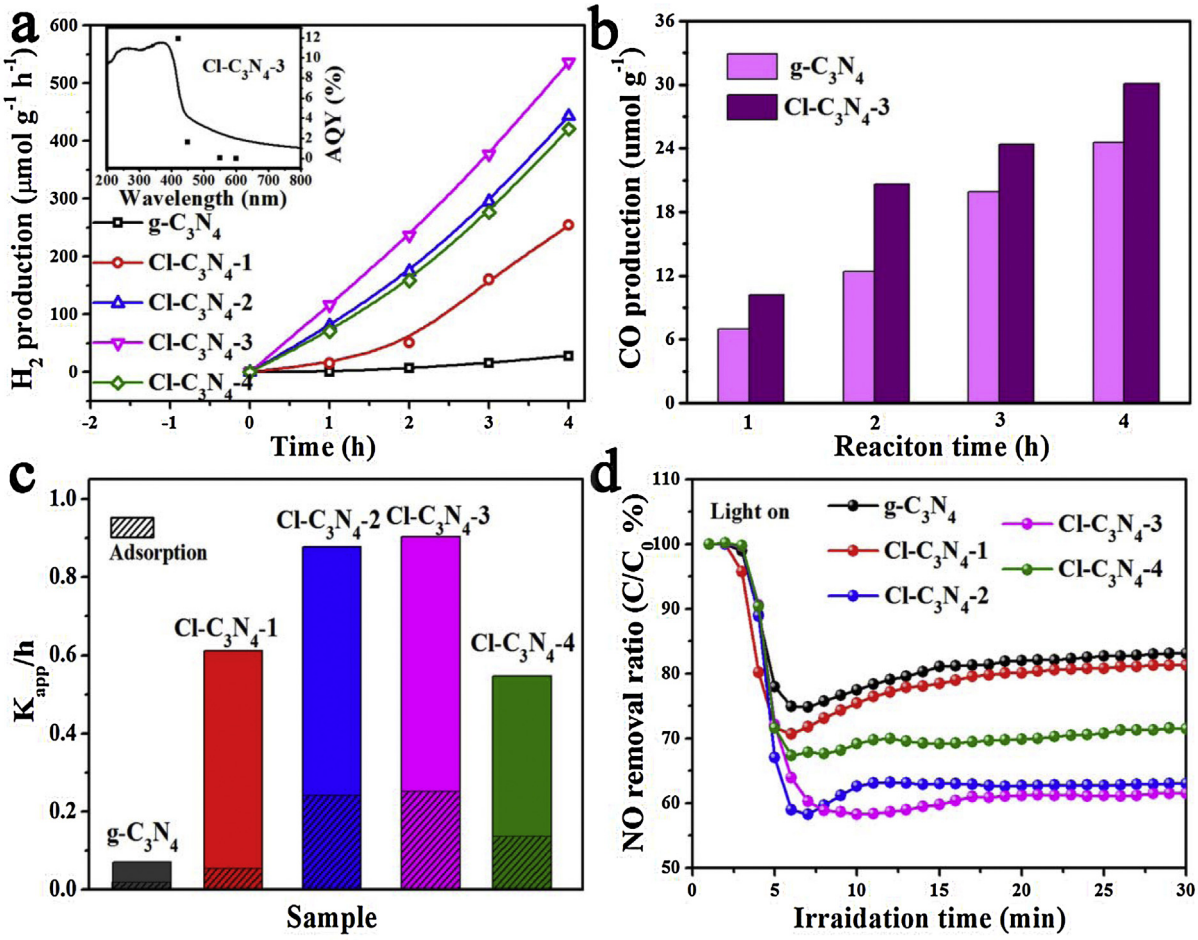

Fig. 5. (a) Photocatalytic H_2 evolution over g-C_3N_4 and Cl-C_3N_4 samples, (b) CO evolution rates from CO_2 by Cl-CN-3 and pure g-C_3N_4, (c) apparent rate constants for degradation of dye model RhB over g-C_3N_4 and Cl-C_3N_4 samples and (d) comparison of NO removal over the g-C_3N_4 and Cl-C_3N_4 samples under visible light irradiation ($\lambda > 420$ nm).

tion rate. Among them, the H_2 evolution rate of Cl-C_3N_4-3 can be increased to 537.1 μmol g^{-1} h^{-1} under the same illuminating conditions, which is almost 19.2 times higher (Fig. S6) than that of pure g-C_3N_4. The inset (Fig. 5a) shows the wavelength-dependent apparent quantum yield (AQY) values on account of H_2 production under different monochromatic lights. The change tendency of AQY data for Cl-C_3N_4-3 sample almost matches with itself DRS curve, and AQY gives impressive values up to 11.9% under a band-pass filter with 420 nm. Besides, we also compare the AQY of Cl intercalated g-C_3N_4 with that of related modified g-C_3N_4 from previously reported literatures. The AQY of 11.9% of this work is comparable with previously reported oxygen-modified g-C_3N_4 (13.7% of AQY at 420 nm) [28]. Furthermore, Qu et al. [29] reported that the AQY of mesoporous nanomesh g-C_3N_4 is 5.1% at 420 nm, which is much smaller than that of Cl intercalated g-C_3N_4, further confirming the superiority of our Cl intercalated g-C_3N_4. The stability of photocatalysts toward H_2 evolution of four consecutive operations is detected. As depicted in Fig. S7, Cl-g-C_3N_4 keeps its high photoreduction activity without evident deactivation after four circulation tests. The XRD analysis (Fig. S8) on the CN-Cl-3 sample before and after above stability test suggests that the structure and phase have no substantial changes except Pt phase, which act as co-catalyst in water splitting process. The widespread attention about photocatalytic reduction of CO_2 is stimulated by the urgent need to minimize greenhouse gas emissions and to produce fuels. Fig. 5b shows the CO_2 evolved rates of Cl-C_3N_4-3, which also exhibits enhanced CO_2 reduction ability compared with pure g-C_3N_4. In comparison with the reaction rates of CO_2 reduction, hydrogen evolution rate presents a much larger enhancement, which may be ascribed that water splitting is a liquid reaction with sufficient contact between photocatalysts and contaminants.

Azo dye model RhB is positively charged and g-C_3N_4 is negatively charged, spontaneous adsorption thus can be realized between RhB and g-C_3N_4, and this characteristic can reflect the variation of specific surface area of photocatalysts. This is the reason why we employ the model dye of RhB rather than other dyes or phenolic contaminants. Fig. 5c illustrates the apparent rate constants of RhB adsorption and degradation. Compared to the pristine g-C_3N_4, Cl-C_3N_4 samples parade not only enhanced adsorption ability, but also significantly boosted photooxidation degradation rates, in which the activity obtained for Cl-C_3N_4-3 displays a 12.9-fold enhancement compared to unmodified g-C_3N_4. Furthermore, the removal of NO in air of g-C_3N_4 and Cl-C_3N_4 samples (Fig. 5d) has been also tested, and the removal ratios reach a maximum in 5 min and then tend towards stability with the following irradiation time. It is found that all modified samples exhibit strengthened activity, and Cl-C_3N_4-3 possesses the highest NO removal ratio. This phenomenon accord with the above photocatalytic H_2 evolution, CO_2 reduction and RhB photodegradation results. Thus, we can conclude that both the photooxidation and photoreduction capabilities of g-C_3N_4 are greatly promoted by Cl intercalation.

As the photocatalytic performance of semiconductors is closely associated with the charge separation efficiency and their band structure, we herein employed both experimental and DFT meth-

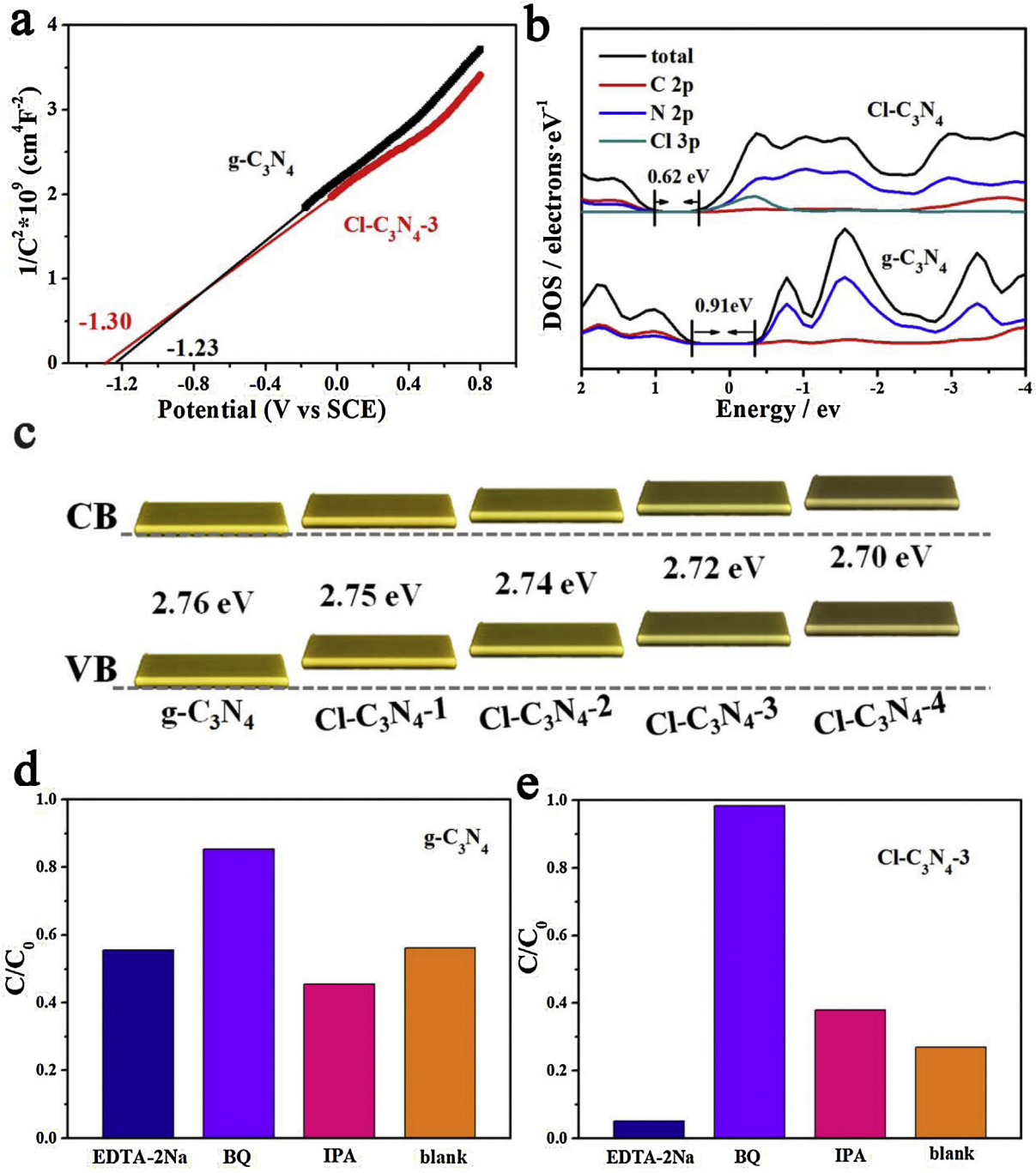

Fig. 6. (a) Mott-Schottky curves of pristine g-C_3N_4 and Cl-C_3N_4-3. (b) Total and partial density of state (DOS) of Cl-C_3N_4. (c) Schematic of band gap energy level of g-C_3N_4 and a series of Cl-C_3N_4-X (X = 1, 2, 3, 4). Photocatalytic degradation efficiencies of RhB over (d) pristine g-C_3N_4 and (e) Cl-C_3N_4-3 alone and with adding scavangers of BQ, IPA, and EDTA-2Na.

ods to investigate the change of these factors. Mott- Schottky plots are obtained to determine the flat band potential and thereby to estimate the band energy levels (Fig. 6a). The positive slopes of Mott-Schottky curves indicate the typical n-type semiconductor characteristics of g-C_3N_4 and Cl modified g-C_3N_4 [30]. The flat-band potentials are separately determined to be −1.23 and −1.30 V (vs SCE) for the pristine g-C_3N_4 and Cl-C_3N_4-3, which equal to −0.99 and −1.06 V (vs NHE), respectively. Generally, the conduction band (CB) position is 0.1–0.3 eV higher than the flat-band potential for n-type semiconductor [31]. So the CB for pristine g-C_3N_4 and Cl-C_3N_4-3 are estimated to be −1.09 and −1.16 eV, respectively. Accordingly, the valence band positions are separately calculated as 1.67 and 1.56 eV based on their band gaps. This result indicates that Cl intercalation could result in the up-shift of CB and VB levels. For further confirmation, DFT calculations on the total and partial density of states are performed. As seen from Fig. 6b, the band gap of Cl-C_3N_4 is clearly narrowed, and the rising of both CB and VB positions can also be observed, verifying the Mott-Schottky result. The up-shift of CB level is believed to be favorable for the generation of photoelectrons with more powerful reducing-ability and more strong-oxidating superoxide radicals ($\bullet O_2^-$). Based on the above experiments results and mechanism calculation, the schematic of band gap energy level of g-C_3N_4 and a series of Cl-C_3N_4-X (X = 1, 2, 3, 4) are depicted and shown in Fig. 6c. Since the generation of reac-

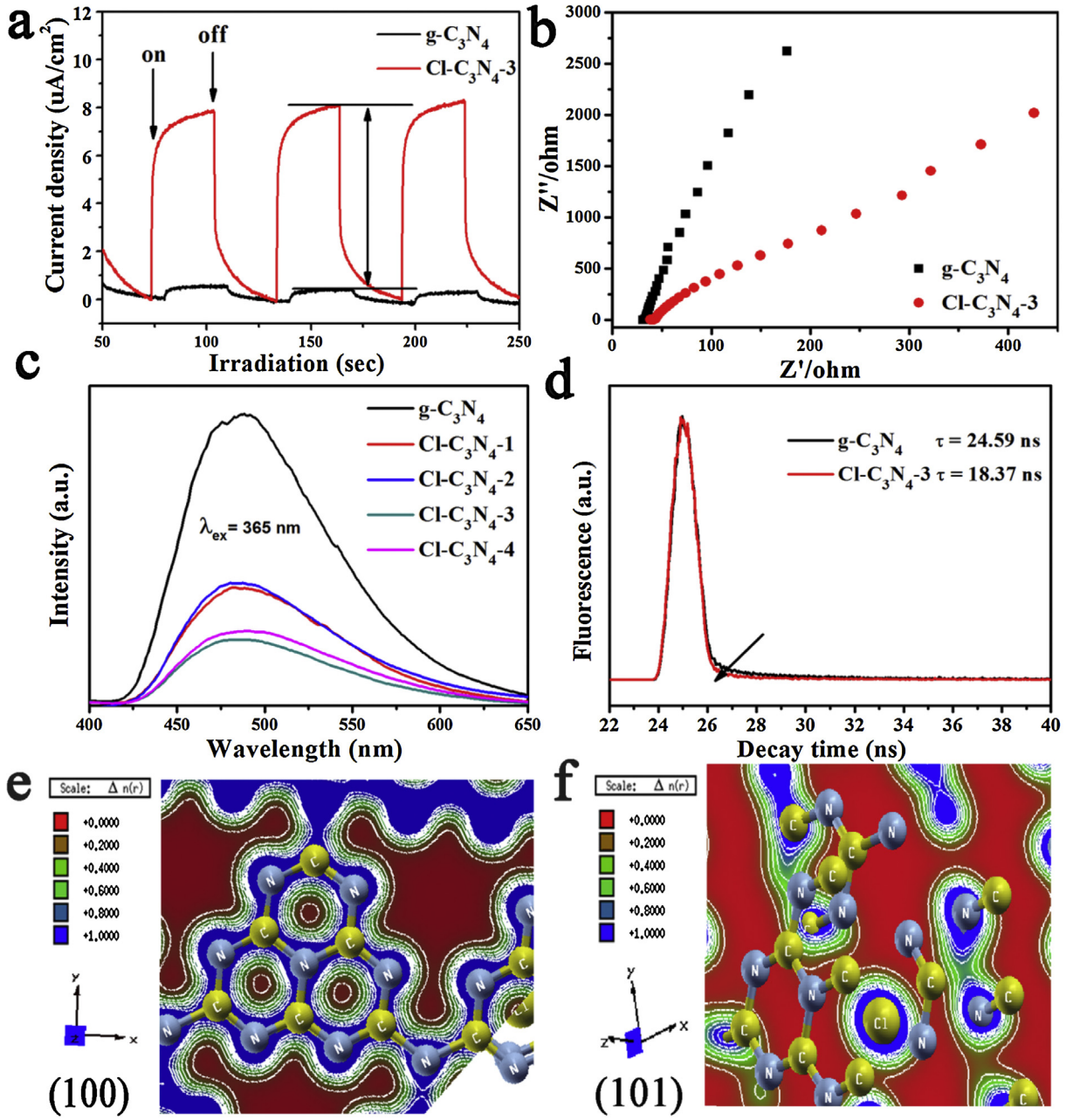

Fig. 7. (a) Transient photocurrent responses and (b) EIS Nyquist plotsof g-C_3N_4 and Cl-C_3N_4-3. (c) Photoluminescence spectra of pristine g-C_3N_4 and Cl intercalated g-C_3N_4 samples. (d) The fitting curves of fluorescence decay of g-C_3N_4 and Cl-C_3N_4-3. Valence charge density in (e) (100) and (f) (101) crystallographic planes of Cl-C_3N_4-3.

tive radicals is tightly related to band energy levels, active species trapping experiments were performed over pristine g-C_3N_4 and Cl-C_3N_4-3 to verify the above band structure modulation (Fig. 6d and e). Scavengers of ethylenediaminetetraacetic acid disodium salt (EDTA-2Na), Benzoquinone (BQ), and isopropanol (IPA) were introduced to detect holes (h^+), $^{\bullet}O_2^-$ and hydroxyl radicals ($^{\bullet}OH$), respectively [32,33]. Compared to pristine g-C_3N_4, the influence of $^{\bullet}O_2^-$ generated by Cl-C_3N_4-3 on degradation is notably strengthened. It reflects the enhanced reduction ability of photogenerated electrons. Meanwhile, the trapping of h^+ by EDTA-2Na conversely promotes the decomposition of RhB, implying that the oxidation ability of h^+ has been weakened. These evidences strongly corroborate that the CB and VB levels are upshifted by Cl intercalation.

Photocurrent generation is applied to investigate the separation efficiency of charge carriers occurred at the interface between photocatalysts and electrolyte [34]. As shown in Fig. 7a, prompt photocurrent responses are observed for g-C_3N_4 and Cl-C_3N_4-3 electrodes, which reveal their sensitive photoelectronic activities. Compared to g-C_3N_4, Cl-C_3N_4-3 exhibits drastically enhanced photocurrent intensity, which is 14 times higher than that of un-modified g-C_3N_4, demonstrating its greatly enhanced charge separation efficiency. Besides, no photocurrent decay occurs during illuminating process, implying that less recombination rate of electron-holes pairs occur. Electrochemical impedance spectra (EIS) can be utilized to elucidate the charge migration behavior [35]. In general, a smaller arc radius in EIS plot reflects a higher efficiency of interfacial charge transfer. It is obvious to find that the arc radius of Cl-C_3N_4-3 is overwhelmingly smaller than that of g-C_3N_4 (Fig. 7b), suggesting that Cl intercalation could profoundly facilitate the high charge transport of g-C_3N_4 [36]. Photoluminescence (PL)

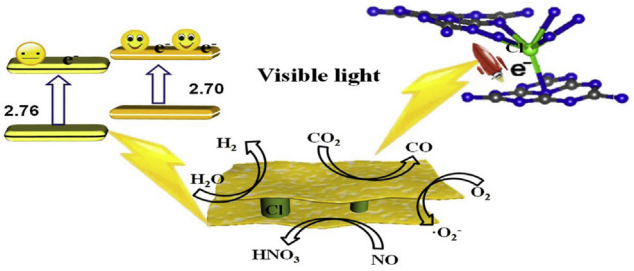

Fig. 8. Schematic diagrams of charge transfer and photocatalytic mechanism of Cl intercalated g-C_3N_4 under visible light irradiation.

spectra are recorded to monitor the recombination rate of photogenerated electrons and holes in the samples. The PL intensities of Cl-C_3N_4 samples are found to be greatly lowered in comparison with that of g-C_3N_4 (Fig. 7c), which reflects that the charge carrier recombination is partially suppressed by Cl doping [37,38]. Time-resolved PL spectra acting as a quantificational solid are developed to confirm the above results [39]. As seen from Fig. 7d, the fluorescence lifetime of Cl-C_3N_4-3 is determined to be 18.37 ns, shorter than that of pristine g-C_3N_4 (24.59 ns). It signifies that the embedded Cl can serve as a channel to efficiently detach and transport the charge carriers between interlayer, which are more prone to be transformed into active radicals to promote the photochemical reactions. This phenomenon has also been reported by Dong et al. [40] and Li et al. [41].

The bonding nature can be accurately explained on the base of electronic charge density plot which is derived from the reliable converge wave function [42,43]. We have calculated the valence charge density in (100) and (101) crystallographic planes for Cl-C_3N_4 which perfectly describe the bonding nature and charge transfer as shown in Fig. 7e and f. It is clear that the (100) crystallographic plane exhibits C and N atoms. The electro-negativities of C and N are 2.55 and 3.04, and the low electro-negativity difference between C and N atoms points to an almost non-polar covalent bond with only 9% of ionic character [44]. The blue color (Fig. 7e and f) shows the maximum charge intensity as shown by the thermo-scale while the red color represents zero charge density regions. Therefore, the charge density distribution in the center of the hexagon is zero. The blue region in the hexagon represents strong sharing of charge between C and N atom which results the dominant covalent bond. One can also observe the bonding nature and percentage iconicity by using Pauling scale and Pauling empirical formula [45]. Fig. 7f illustrates (101) crystallographic plane which shows all atoms. It has been found that the Cl atom surrounds by uniform spheres of charge density and the maximum accumulates around Cl atom. This implies that efficient charge transfer occurs towards Cl atom. Thus, the Cl intercalation efficaciously extends the local 2D π-conjugated system of g-C_3N_4 into three-dimensional space and subsequently promotes the separation and mobility of charge carriers.

Based on the aforementioned experimental and theoretical results, the photocatalytic mechanism of efficient H_2 evolution, CO_2 reduction, NO removal, and dye degradation as well as the charge transfer process induced by Cl intercalation are proposed as illustrated in Fig. 8: Firstly, via constructing charge transport channel, the intercalated Cl extends the local 2D π-conjugated system of g-C_3N_4 and thereby results in enhanced electronic delocalization, which greatly facilitates the separation and mobility of charge carriers along the layers. Secondly, up-shift of the conduction band potential provides the g-C_3N_4 material a stronger reduction ability of the photogenerated electrons and also a stronger oxidation ability of the as-formed superoxide radicals $^{\bullet}O_2^-$, respectively, leading to an enhancement of the photoreduction and photooxidation activity. Moreover, the narrowed band gap allows g-C_3N_4 to utilize more efficiently visible light to activate more photoinduced charge carriers participating in the photochemical reactions. Finally, the treatment by excessive ammonium chloride offers abundant gas soft-template resulting in porous g-C_3N_4 products, which provides increased specific surface area and more active reaction sites, accelerating the photocatalytic reaction process.

4. Conclusions

In summary, we developed Cl intercalated g-C_3N_4 by a substantial-ammonium chloride assisted soaking-pyrolysis method. Compared with pristine g-C_3N_4, the Cl-g-C_3N_4 unfolds distinguished photocatalytic performance. The H_2 evolution rate enhances 19.2-fold with an apparent quantum efficiency of 11.9% at 420 ± 15 nm, and it also shows superior abilities on photocatalytic CO_2 reduction, removal of azo model dye RhB and gaseous NO. It is demonstrated that the highly facilitated separation and transfer of electron-hole pairs, more negative CB position, narrowed energy gap and enlarged specific surface area are responsible for the drastically enhanced photoactivity, as evidenced by both experimental and theoretical results. This study not only paves a new way for further development of g-C_3N_4 for future practical applications, but also advances our understanding on the modification of 2D materials by simple approaches.

Acknowledgements

This work was supported by the National Natural Science Foundations of China (Grant No. 51672258, No. 51302251 and No. 51572246), the Fundamental Research Funds for the Central Universities (No. 2652015296). CENTEM project CZ.1.05/2.1.00/03.0088, CENTEM PLUS (LO1402), MetaCentrum (LM2010005) and CERIT-SC (CZ.1.05/3.2.00/08.0144)

Appendix A. Supplementary data

Supplementary data associated with this article can be found, in the online version, at http://dx.doi.org/10.1016/j.apcatb.2016.10.002.

References

[1] L.V. Lightcap, P.V. Kamat, Acc. Chem. Res. 46 (2013) 2235–2243.
[2] L.V. Lightcap, T.H. Kosel, P.V. Kamat, Nano Lett. 10 (2010) 577–583.
[3] X.C. Wang, K. Maeda, A. Thomas, K. Takanabe, G. Xin, J.M. Carlsson, K. Domen, M. Antonietti, Nat. Mater. 8 (2009) 76–80.
[4] Q.H. Wang, K. Kalantar-Zadeh, A. Kis, J.N. Coleman, M.S. Strano, Nat. Nanotechnol. 7 (2012) 699–712.
[5] X.C. Wang, X.F. Chen, A. Thomas, X.Z. Fu, M. Antonietti, Adv. Mater. 21 (2009) 1609–1612.
[6] J. Mao, T.Y. Peng, X.H. Zhang, K. Li, L.Q. Ye, L. Zan, Catal. Sci. Technol. 3 (2013) 1253–1260.
[7] Y. Zheng, L.H. Lin, X.J. Ye, F.S. Guo, X.C. Wang, Angew. Chem. Int. Ed. 53 (2014) 11926–11930.
[8] M. Groenewolt, M. Antonietti, Adv. Mater. 17 (2005) 1789–1792.
[9] C.S. Pan, J. Xu, Y.J. Wang, D. Li, Y.F. Zhu, Adv. Funct. Mater. 22 (2012) 1518–1524.
[10] S.C. Yan, Z.S. Li, Z.G. Zou, Langmuir 26 (2010) 3894–3901.
[11] Y.J. Zhang, T. Mori, J.H. Ye, M. Antonietti, J. Am. Chem. Soc. 132 (2010) 6294–6295.
[12] G. Liu, P. Niu, C.H. Sun, S.C. Smith, Z.G. Chen, G.Q. Lu, H.M. Cheng, J. Am. Chem. Soc. 132 (2010) 11642–11648.
[13] G.H. Dong, K. Zhao, L.Z. Zhang, Chem. Commun. 48 (2012) 6178–6180.
[14] J.H. Li, B. Shen, Z.H. Hong, B.Z. Lin, B.F. Gao, Y.L. Chen, Chem. Commun. 48 (2012) 12017–12019.
[15] L. Xu, J.X. Xia, H. Xu, J. Qian, J. Yan, L.G. Wang, K. Wang, H.M. Li, Analyst 138 (2013) 6721–6726.
[16] Q. Liu, J.Y. Zhang, Langmuir 29 (2013) 3821–3828.
[17] T. Xiong, W.L. Cen, Y.X. Zhang, F. Dong, ACS Catal. 6 (2016) 2462–2472.
[18] X. Lu, K. Xu, P. Chen, K. Jia, S. Liu, C. Wu, J. Mater. Chem. A 2 (2014) 18924.
[19] J. Wan, S.Z. Hu, F.Y. Li, Z.P. Fan, F. Wang, J. Zhang, Asian J. Chem. 26 (2014) 8543–8546.

[20] J.P. Perdew, K. Burke, M. Ernzerhof, Phys. Rev. Lett. 77 (1996) 3865–3868.
[21] M.D. Segall, P.L.D. Lindan, M.J. Probert, C.J. Pickard, P.J. Hasnip, S.J. Clark, M.C.J. Payne, Phys. Condens. Matter. 14 (2002) 2717–2744.
[22] Z.D. Huang, M. Wen, Q.S. Wu, Y.Q. Zhang, H. Fang, H.X. Chen, J. Colloid Interface Sci. 460 (2015) 230–236.
[23] F. Dong, M.Y. Ou, Y.K. Jiang, S. Guo, Z.B. Wu, Ind. Eng. Chem. Res. 53 (2014) 2318–2330.
[24] L.H. Yao, D. Wei, Y.M. Ni, D.P. Yan, C.W. Hu, Nano Energy 26 (2016) 248–256.
[25] H.W. Huang, X.W. Li, J.J. Wang, F. Dong, P.K. Chu, T.R. Zhang, Y.H. Zhang, ACS Catal. 5 (2015) 4094–4103.
[26] H.W. Huang, Y. He, Z.S. Lin, L. Kang, Y.H. Zhang, J. Phys. Chem. C 117 (2013) 22986–22994.
[27] Y.P. Zhu, T.Z. Ren, Z.Y. Yuan, ACS Appl. Mater. Interfaces 7 (2015) 16850–16856.
[28] X.J. She, J.J. Wu, J. Zhong, H. Xu, Y.C. Yang, R. Vajtai, J. Lou, Y. Liu, D.L. Du, H.M. Li, P.M. Ajayan, Nano Energy 27 (2016) 138–146.
[29] Q. Han, B. Wang, J. Gao, Z.H. Cheng, Y. Zhao, Z.P. Zhang, L.T. Qu, ACS Nano 10 (2016) 2745–2751.
[30] J. Zhang, X. Chen, K. Takanabe, K. Maeda, K. Domen, J.D. Epping, X. Fu, M. Antonietti, X. Wang, Angew. Chem. Int. Ed. 49 (2010) 441–444.
[31] H. Kim, P. Borse, W. Choi, J. Lee, Angew. Chem. Int. Ed. 44 (2005) 4585–4589.
[32] P. Ji, J. Zhang, F. Chen, M. Anpo, B: Appl. Catal. 85 (2009) 148–154.
[33] M. Yin, Z. Li, J. Kou, Z. Zou, Environ. Sci. Technol. 43 (2009) 8361–8366.
[34] H.W. Huang, K. Xiao, Y. He, T.R. Zhang, F. Dong, X. Du, Y.H. Zhang, B: Appl. Catal. 199 (2016) 75–86.
[35] G.G. Zhang, M.W. Zhang, X.X. Ye, X.Q. Qiu, S. Lin, X.C. Wang, Adv. Mater. 26 (2014) 805–809.
[36] X.J. Bai, R.L. Zong, C.X. Li, D. Liu, Y.F. Liu, Y.F. Zhu, Appl. Catal. B: Environ. 147 (2014) 82–91.
[37] H.W. Huang, X. Han, X.W. Li, S.C. Wang, P.K. Chu, Y.H. Zhang, ACS Appl. Mater. Interfaces 7 (2015) 482–492.
[38] H.W. Huang, K. Liu, K. Chen, Y.L. Zhang, Y.H. Zhang, S.C. Wang, J. Phys. Chem. C 118 (2014) 14379–14387.
[39] X.B. Li, G. Hartley, A.J. Ward, P.A. Young, A.F. Masters, T. Maschmeyer, J. Phys. Chem. C 119 (2015) 14938–14946.
[40] F. Dong, Z. Zhao, Y. Sun, Y. Zhang, S. Yan, Z. Wu, Environ. Sci. Technol. 49 (2015) 12432–12440.
[41] Y. Li, H. Xu, S. Ouyang, D. Lu, X. Wang, D. Wang, J. Ye, J. Mater. Chem. A 4 (2016) 2943–2950.
[42] R. Hoffman, Rev. Mod. Phys. 60 (1988) 601.
[43] C.D. Gellatt, A.R.J. Willaims, V.L. Moruzzi, B: Phys. Rev. 27 (1983) 2005.
[44] F.M. Gao, J.L. He, E. Wu, S.M. Liu, D.L. Yu, D.C. Li, S.Y. Zhang, Y. Tian, J. Phys. Rev. Lett. 91 (2003) 015502.
[45] Schlusseltechnologien Key Technologies, 41st IFF Springschool, 2010, pp A1.18.